Mat. Res. Soc. Symp. Proc. Vol. 692 © 2002 Materials Research Society

Sb-Based Mid-Infrared Diode Lasers

C. Mermelstein, M. Rattunde, J. Schmitz, S. Simanowski, R. Kiefer, M. Walther, and J. Wagner
Fraunhofer-Institut für Angewandte Festkörperphysik,
Tullastrasse 72, D-79108 Freiburg, Germany

ABSTRACT

In this paper we review recent progress achieved in our development of type-I GaInAsSb/AlGaAsSb quantum-well (QW) lasers with emission wavelength in the 1.74-2.34 μm range. Triple-QW (3-QW) and single-QW (SQW) diode lasers having broadened waveguide design emitting around 2.26 μm have been studied in particular. Comparing the two designs we have find that the threshold current density at infinite cavity length as well as the transparency current density scale with the number of QWs. Maximum cw operating temperature exceeding 50°C and 90°C has been obtained for ridge waveguide lasers emitting above and below 2 μm, respectively. Ridge waveguide diode lasers emitting at 1.94 μm exhibited internal quantum efficiencies in excess of 77%, internal losses of 6 cm^{-1}, and threshold current density at infinite cavity length as low as 121 A/cm^2 reflecting the superior quality of our diode lasers, all values recorded at 280 K. A high characteristic temperature T_0 of 179 K for the threshold current along with a value of T_1 = 433 K for the characteristic temperature of the external efficiency have been attained for the 250-280 K temperature interval. Room temperature cw output powers exceeding 1.7 W have been demonstrated for broad area single element devices with high-reflection/antireflection coated mirror facets, mounted epi-side down. The latter result is a proof for the high power capabilities of these GaSb-based mid-ir diode lasers.

INTRODUCTION

Semiconductor diode lasers emitting at wavelengths around 2 μm and beyond are of significant current interest for an increasing number of applications, including tunable diode laser absorption spectroscopy (TDLAS) for process control and environmental monitoring, as well as materials processing such as welding of plastics and medical laser surgery. Many of the potential applications for mid-ir semiconductor lasers, in particular those involving molecular spectroscopy and remote sensing, require coherent sources with narrow linewidths. While the TDLAS related applications ask for high spectral purity and tunability of the diode laser, the two latter applications call for high output powers on the multiple watt level and concomitant high power conversion efficiency along with good beam quality. An additional key issue is the ambient or above ambient operating temperatures while maintaining high power efficiency. For the 2-3 μm wavelength interval, the conventional interband diode laser approach is adopted, employing GaInAsSb/AlGaAsSb type-I QW/barrier layers as active region grown on GaSb substrates [1, 2]. Diode lasers based on the (AlGaIn)(AsSb) material system covering the above given spectral range demonstrated excellent room temperature performances, including very low threshold current density (J_{th}), very low internal loss coefficient, and high internal quantum efficiency [3-7]. Furthermore, cw output power of 1.9 W at 15°C has been obtained from 200 μm x 2 mm broad area diode lasers emitting at 2 μm [4].

In this paper we give an overview of our results regarding the development of GaInAsSb/AlGaAsSb type-I diode lasers emitting between 1.74 and 2.34 μm, already published in part in Ref. 8-

11. The diode lasers studied in this work are based on the broadened waveguide separate confinement heterostructure concept.

EXPERIMENT

All diode laser structures described in the present paper were grown on commercial 2-inch (100) n-type GaSb:Te substrates in a solid-source molecular beam epitaxy system equipped with valved cracker effusion cells for the group V elements producing beams of As_2 and Sb_2 . The epitaxial layer sequence starts with an n^+-GaSb:Te buffer layer, followed by an n-type digitally graded GaSb/AlGaAsSb SL transition region towards the 2 μm thick n-$Al_{0.85}Ga_{0.15}As_{0.07}Sb_{0.93}$ bottom optical cladding layer nominally lattice matched to the GaSb buffer layer. The active region of the 3-QW laser consists of three compressively strained 10 nm thick undoped $Ga_{0.70}In_{0.30}As_{0.06}Sb_{0.94}$ QWs separated by 20 nm wide undoped $Al_{0.28}Ga_{0.72}As_{0.02}Sb_{0.98}$ barriers lattice matched to the GaSb substrate. The QW region is embedded between 400 nm thick $Al_{0.28}Ga_{0.72}As_{0.02}Sb_{0.98}$ separate confinement layers, resulting in a total waveguide thickness of 870 nm. The layer sequence is completed by a 2 μm wide p-$Al_{0.85}Ga_{0.15}As_{0.07}Sb_{0.93}$ upper optical cladding layer followed by a p-type digitally graded GaSb/AlGaAsSb SL transition region towards the p^+-GaSb:Be contact layer. The single QW laser incorporates 480 nm thick separate confinement layers and one QW in the active region, while the other parts of the structure are identical to the 3-QW laser. The entire active region and the top cladding layer are grown at a temperature of ~ 470°C, while the bottom cladding layer at a higher temperature of ~ 550°C. For more details regarding the growth conditions see [8, 9]. An additional set of ten diode lasers all comprising 3 QWs have been grown where the only parameters intentionally varied were the In and As contents in the QWs, from 0.07 to 0.30 and from 0 to 0.15, respectively. All other parts of the layer sequence are identical with the above mentioned structure. The energy band-edge profile of a typical 3-QW layer sequences, calculated using the Model Solid Theory [12], is shown in Figure 1.

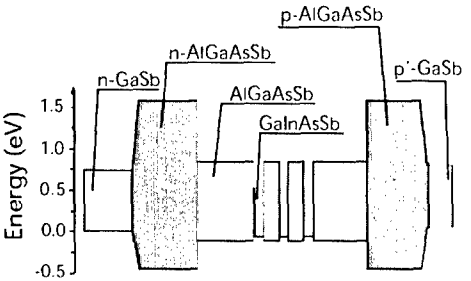

Figure 1. Schematic energy band-edge profile of a 3-QW laser structure.

After the growth the epitaxial layer structures were analyzed by high-resolution X-ray diffraction (HRXRD) and secondary ion mass spectroscopy (SIMS) in order to determine the individual layer compositions, as well as doping concentrations. Figure 2 displays a typical HRXRD profile covering the 004 reflection range of GaSb for a 3-QW diode laser. The diagram reveals well-resolved SL diffraction peak signature of the 3 QW active region along with narrow diffraction peaks associated with the AlGaAsSb cladding and separate confinement layers. The difference between the zero-order SL peak

and the GaSb buffer peak provides the net strain in the SL. In this case the zero-order peak of the SL is shifted to a diffraction angle smaller than that of the GaSb buffer layer, reflecting a compressively strained SL with $\Delta a/a = 9.5 \times 10^{-3}$. As clearly seen, the measured data are in good agreement with the simulation. The residual mismatch of both cladding layers was in most cases below 1×10^{-3}, indicating excellent lattice matching and thus high crystalline quality. All in all, these laser structures show a superior material quality indicative for our mature growth technique.

SIMS depth profiles of the group III elemental components Al, Ga, and In, along with those of the dopants Be and Te are plotted in Figure 3. The Ga and Al depth profiles clearly mark the cladding and the separate confinement layers, while the In depth profile shows the QW region. Each dopant profile was calibrated against known implants into AlGaAsSb. It can be seen that the cladding layers are heavily doped in order to minimize Ohmic losses, typically the Be is incorporated up to a level of 5.5×10^{18} cm^{-3}, and the Te doping level is higher with a concentration of 1.4×10^{19} cm^{-3}.

Edge-emitting index-guided Fabry-Perot diode lasers with ridge aperture varying from 6 to 64 μm have been prepared for all the structures reported in this paper, using standard optical lithography and chemically assisted ion beam etching. For high output power gain guided 150 μm broad area lasers separated by trench etch isolation have been fabricated. In the latter devices the cap etching was done by selective reactive ion etching. The etched surfaces were passivated with SiN. Ti/Pt/Au and (AuSn)Au have been deposited for the top p-contact and backside n-contact metalization, respectively. Laser bars with cavity lengths varying between 0.5 and 2 mm have been cleaved and soldered either substrate-side down or, for high output powers, epi-side down onto copper heat sink. For several laser bars, to maximize single ended output, low-reflectivity, AR (5%), and high-reflectivity, HR (95%), coatings have been applied to the cleaved mirror facets. The emission spectra were measured by focusing the laser beam into a Fourier-transform infrared (FTIR) spectrometer equipped with a cooled InSb detector, using f/4 collection optics and spectral resolution of 0.25 cm^{-1} (~1 Å). For absolute light-power measurements the lasing emission was collected into a calibrated pyroelectric detector.

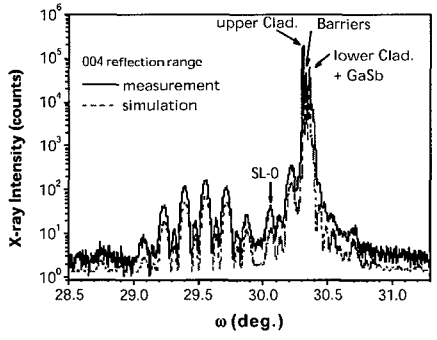

Figure 2. Experimental HRXRD profile (upper curve) and simulated profile (lower curve) covering the 004 reflection range of GaSb for a 3-QW diode laser structure.

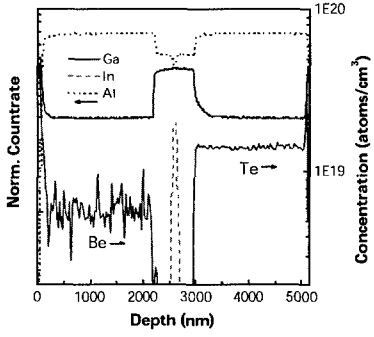

Figure 3. SIMS depth profiles of individual elemental constituents Al, Ga and In (left axis), and of the p and n dopants Be and Te, respectively (right axis), for a 3-QW laser.

RESULTS AND DISCUSSION

3-QW and SQW diode lasers emitting at 2.26 μm

The room temperature current-voltage characteristics of the devices revealed turn-on voltages around 0.7 V and low series resistances of about 300 mΩ for 64 μm x 1000 μm ridge waveguide lasers. All laser diodes were electro-optically characterized in cw operation. Additionally, for an accurate determination of the threshold current pulsed mode measurements have been performed. Current pulses of 5 μs duration at a 10 kHz repetition rate were generated by a Fastest pulsed current source. The light output power as a function of the injection current was measured at heat sink temperatures varying between 250 and 360 K for several ridge widths and cavity lengths. The power levels quoted below have been corrected for the transmission coefficients of the output optics and for the collection efficiency. Figure 4 shows cw collected optical power from a single facet and total power efficiency versus drive current, for a 64 μm x 600 μm 3-QW ridge-waveguide laser recorded at 280 and 310 K. A differential quantum efficiency (η_d) of 50% and a total power efficiency (called also wall-plug efficiency) of 23% were deduced at 280 K. The latter is the highest value reported so far for diode lasers emitting beyond 2.2 μm and equals the power efficiency of 22.5% reported for a single-QW GaInAsSb/AlGaAsSb laser with a significantly shorter emission wavelength of 2.05 μm [3]. The relatively high power conversion efficiency reflects the high η_d and low series resistance achieved for the present lasers.

The spectral characterization in cw mode yielded single mode lasing emission at several temperatures for drive currents near threshold. The inset of Figure 4 shows high-resolution single longitudinal mode cw lasing spectra, recorded at 280 and 310 K, for a 64 μm x 600 μm 3-QW diode laser, with emission close to 2.26 μm for the latter temperature. At higher injection currents the lasing spectrum exhibited multiple longitudinal modes. The temperature dependence of the lasing emission yielded a temperature tunability rate of ~ 1.3 nm/°C, a property linked to the temperature sensitivity of the GaInAsSb band gap. As the cavity length (L) is decreased from 1250 to 500 μm, the peak emission

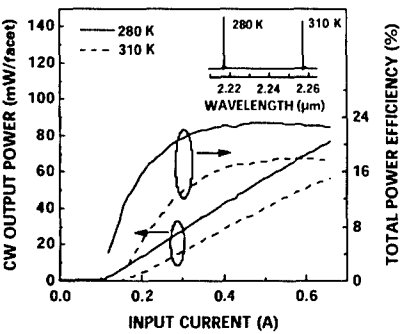

Figure 4. CW light output power per facet and total power efficiency vs injection current of a 64 μm x 600 μm 3-QW ridge laser operated at 280 and 310 K. The inset displays high resolution spectra of single longitudinal mode laser emission at the mentioned operating temperatures.

wavelength for cw operation at room-temperature decreases from 2.26 to 2.23 μm, as a result of increased band filling due to higher threshold carrier densities at shorter cavity lengths.

The threshold currents (I_{th}) are plotted as a function of the cavity length in inset of Figure 5 for the 3-QW and SQW lasers at 280 K. A linear decrease with L down to 550 μm and 1200 μm is observed for the 3-QW and SQW lasers, respectively. Further decrease in L leads to a stagnation in I_{th} due to gain saturation [13]. This behavior is more pronounced for the SQW than for the 3-QW laser due to the reduced number of QWs. Furthermore, for the SQW laser even an increase in I_{th} is noticed for the two shortest cavity lengths. The temperature sensitivity of I_{th} in the 200 - 280 K thermal range can be described by a characteristic temperature of T_O = 110 K for the 3-QW laser.

Figure 5 depicts J_{th} versus reciprocal cavity length (1/L) together with a linear fit to the experimental data for the 3-QW and SQW lasers, both with 64 μm apertures, recorded at 280 K. Values as low as 117 A/cm^2 and 199 A/cm^2 (corresponding to 66 A/cm^2 per QW) have been achieved for the SQW and 3-QW lasers, respectively, both with 2 mm cavity length. These values compare favorably well with the 230 A/cm^2 (115 A/cm^2 per QW) reported for a double-QW laser at 2.3 μm [7]. The linear fit to the experimental data results in a J_{th} at infinite cavity of 150 A/cm^2 for the 3-QW and a value about a factor of three smaller, 55 A/cm^2, for the SQW, as expected from the decreased number of QWs. Note that for the linear fit of the SQW data the three shortest cavity lengths were ignored because of gain saturation, as discussed above.

To deduce the standard laser parameters, namely the internal quantum efficiency (η_i) and internal loss coefficient (α_i), the inverse of η_d is plotted against the cavity length, illustrated in the inset of Figure 6 for the SQW laser with a 64 μm aperture. The η_i and α_i values were derived using the relation $\eta_d=\eta_i /[1+\alpha_i L/\ln(1/R)]$. The linear fit results in high η_i-values of 69% and 65% for 3-QW and SQW, respectively, and α_i as low as of 7.7 cm^{-1} (3-QW) and 5 cm^{-1} (SQW). The lower loss coefficient of the SQW laser is attributed to the reduced number of interfaces in the active region. For the fit to the SQW the data point at the shortest cavity length was omitted again due to the influence of gain saturation. We point out that the data show a very low scatter even though no data averaging for a given cavity length was performed.

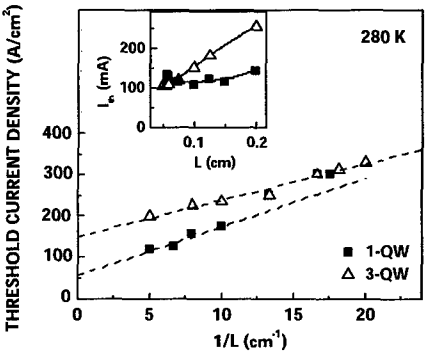

Figure 5. Threshold current density vs inverse cavity length for the 3-QW (triangles) and SQW (squares) diode lasers with 64 μm wide ridges at 280 K. The inset depicts the cavity length dependence of the threshold current for the 3-QW and SQW lasers at 280 K.

The modal gain and the transparency current density have been deduced by computing the total loss for various devices with different L. The current-dependent modal gain derived from the total losses (scattered points) and the logarithmic fit [14] to the experimental data (dashed curves) are depicted in Figure 6, for the SQW (squares) and 3-QW (triangles) lasers at 280 K. Transparency current densities of 41 A/cm^2 and 113 A/cm^2 have been obtained for the SQW and 3-QW lasers, respectively. We point out that these values of transparency current density scale with the number of QWs in the same way as the threshold current density at infinite cavity length, indicating a superior diode laser quality.

1.74 - 2.34 μm 3-QW diode lasers

Furthermore GaInAsSb/AlGaAsSb diode lasers with emission wavelengths varying from 1.74 to 2.34 μm have been investigated. The lasers have been electro-optically characterized in cw operation in order to determine the laser characteristic parameters, namely the characteristic temperature T_0, the internal quantum efficiency η_i, and the internal loss coefficient α_i.

The cw lasing spectra recorded at 280 K heat sink temperature from nine different diode lasers, spanning the 1.84 - 2.34 μm spectral range, is shown in Figure 7. The geometry for all these diode lasers was 64 μm x 600 μm. One major peak, indicating single mode activity, has been observed in lasing spectra of several devices at low injection currents slightly above threshold. However, more peaks, reflecting multi-mode behavior, emerged at larger currents. The inset displays the spectrum of the 2.13 μm diode laser on an expanded wavelength scale. It shows well resolved multiple longitudinal mode emission with mode spacing of ~ 1 nm.

Figure 8 illustrates representative cw power output and total power efficiency plotted versus injection current, recorded at 280 K heat sink temperature for three 64 μm x 1000 μm different diode lasers emitting at 1.94, 2.21 and 2.34 μm. The light output power drops substantially upon increasing the wavelength, so does the power efficiency, due to the increase of Auger losses and QW heterobarrier leakage with increasing wavelength [11]. The maximum output powers are limited by the onset of thermal rollover due to the substrate-side-down mounting of the devices.

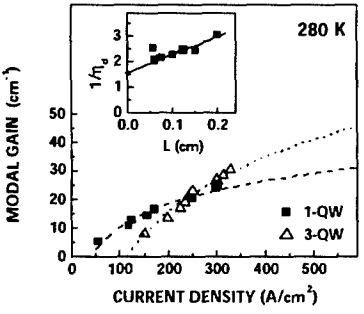

Figure 6. Modal gain vs current density for the 3-QW (triangles) and SQW (squares) diode lasers at 280 K. The inset shows the cavity length dependence of the inverse differential quantum efficiency of the SQW laser at 280 K.

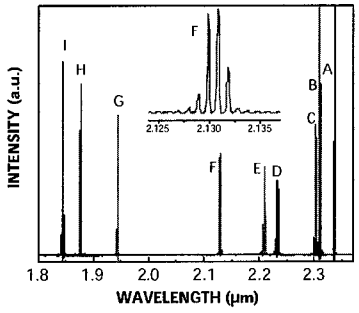

Figure 7. 280 K lasing spectra of nine different diode lasers covering the wavelength interval from 1.84 to 2.34 μm. The inset displays the emission of the 2.13 μm diode laser on an expanded wavelength scale. All lasers in this graph had a 64 μm x 600 μm size.

The maximum output power decreases approximately by a factor of three when proceeding from the shortest to the longest wavelength device, accompanied by a decrease in maximum power efficiency from 29% to 10%. Higher light output powers have been obtained by applying HR/AR coating with reflectivities of 95% and 5%, respectively, to the mirror facets of the lasers.

The characteristic temperature T_O of the threshold current has been studied in more detail by characterizing the devices in cw as well as in pulsed operation. The temperature dependence of the threshold current measured in pulsed mode for 4 different lasers, emitting at 2.34, 2.30, 2.13 and 1.94 μm, is depicted in Figure 9. For the three diode lasers emitting on the short-wavelength side two distinct temperature regimes are visible showing different T_O values. A study regarding the temperature dependence of the threshold current as a function of the wavelength revealed the following results: a decrease in T_O , determined for the low temperature interval, from 179 K to 54 K is obtained for wavelengths increasing from 1.94 μm to 2.34 μm.

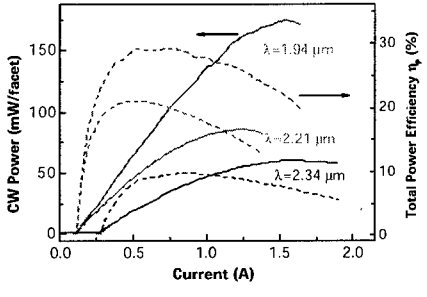

Figure 8. Power output vs current (solid lines) and power efficiency vs current (dashed lines) characteristics recorded at 280 K for three lasers emitting at 1.94, 2.21 and 2.34 μm. The 64 μm x 1000 μm ridge waveguide lasers were operated in cw mode.

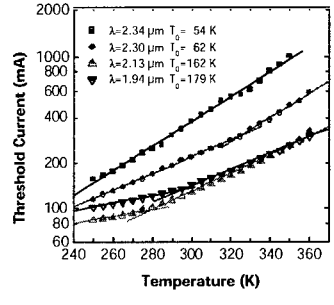

Figure 9. Pulsed threshold current vs temperature for different 64 μm x 1000 μm ridge waveguide lasers with wavelength emission between 1.94 to 2.34 μm. The T_O values for the low temperature range are given as well in the graph.

In order to understand the decrease of T_0 with increasing wavelength, it is necessary to analyze the two main contributions responsible for the temperature sensitivity of I_{th}, namely the Auger recombination and the heterobarrier leakage. For an extensive analysis an additional diode laser, sample J, emitting at the shortest wavelength of 1.7 μm, has been included. The Auger recombination is proportional to $\exp(-\mu E_g/k \cdot T)$ [1], where E_g is the effective band gap energy and μ designates the reduced electron-hole mass. Therefore, if Auger is the dominant loss mechanism then T_0 can be expected to increase with the band gap. To test the validity of this assumption for the present set of lasers, T_0 is plotted in Figure 10 (a) against the emitted photon energy. In order to provide a higher accuracy of the experimental data, T_0 values obtained from pulsed measurements have been used since they are more precise than cw measurements, as the former prevent self-heating of the devices. Indeed, as shown in Figure 10 (a) for samples A to G, an increase in T_0 with respect to the photon energy is observed as expected from the above discussion, but all at once a decrease for lasers H, I and J, emitting on the short-wavelength side, appears which is not consistent with the view of Auger recombination limited threshold current. On the other hand, the heterobarrier leakage is proportional to $m^{-1/2} \cdot \exp(-E_B/kT)$ [15], where E_B is the conduction (ΔE_C) or valence band offset (ΔE_V), whatever is smaller. Therefore, if the heterobarrier leakage is the dominant mechanism, T_0 should increase with E_B. Figure 10 (b) shows the T_0 values as a function of the conduction or valence band offset, whichever is smaller. Within the scatter of the experimental data a monotonic increase of T_0 with increasing band offset is observed, favoring the assumption that heterobarrier leakage is indeed dominant. Detailed studies of GaInAsSb/AlGaAsSb type-I QW diode lasers emitting in the 2.3 to 2.6 μm wavelength range have shown that for 2.3 μm lasers with $\Delta E_C \approx \Delta E_V$, the temperature dependence of I_{th} is governed by nonradiative two-particle recombination [16]. Thence, the current experimental results strengthened by sample J lead us to conclude that of the two mechanisms discussed above, the temperature dependence of I_{th} is governed by heterobarrier leakage, limiting the high-temperature performance of the present diode lasers.

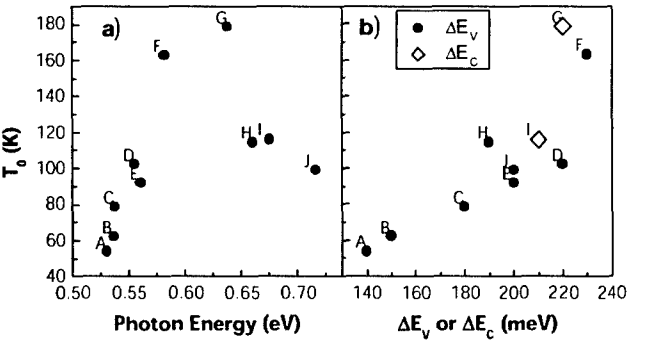

Figure 10. Characteristic temperature T_0 of the different diode lasers vs a) emitted photon energy and b) valence band offset ΔE_V (circles) or conduction band offset ΔE_C (rhombs), whichever is smaller.

Additional laser parameters, derived from the present wavelength series of diode lasers, are shown in Table I, where the values of α_i and η_i as well as the J_{th} for infinite cavity length ($J_{th,\infty}$) are compiled for the various laser structures emitting between 1.87 and 2.34 μm.

The transversal optical field has been calculated taking into account the various refractive indexes of the different epitaxial layers forming the optical waveguide. Figure 11 a) shows the refractive index and the resulting transversal optical mode intensity as a function of the transversal position, corresponding to the growth direction, for two different diode lasers emitting at 1.84 and 2.34 μm. The inset displays the same data on an expanded length scale for the active region. The calculated confinement factor of the QWs (defined by the overlap between the optical mode and the QWs) amounts to 4.7% for the 1.84 μm laser and 4% for the 2.34 μm device. The overlap with the cladding layers was calculated as well, yielding values of 8.7% and 15.5% for the short and long wavelength emitting devices, respectively.

An additional key issue for high power applications is the beam quality. To that purpose the far field (FF) distribution both along the slow and fast axis have been measured. FF scans in the transversal (fast axis) and lateral direction (slow axis) of the laser emission have been performed by rotating the diode laser placed at a distance of 20 cm in front of an extended wavelength InGaAs detector with 1 mm diameter. The diode laser has been operated at two different drive currents, 2 and 4 times the threshold. The device under investigation had a 16 μm x 1000 μm geometry and the mirror facets were HR/AR coated. All the measurements were performed at room temperature. The measured fast axis profiles for the two different injection currents, $2I_{th}$ and $4I_{th}$, were almost identical, exhibiting a Gaussian shape with full-width at half-maximum (FWHM) divergence angle of ~ 67°, which compares well with the calculated value of 60°. Figure 11 b) displays the calculated and measured transversal FF angular distribution for the above mentioned diode lasers, emitting at 1.84 and 2.34 μm. The graph reveals a very good agreement between the calculated and experimental data. In addition, both the calculated and simulated curves show no significant dependence with respect to the wavelength.

Table I. Internal loss coefficient α_i, internal quantum efficiency η_i, as well as threshold current density for infinite cavity length $J_{th,\infty}$ for the various laser diode structures with emission wavelength given in the second column.

Wafer	λ *(μm)*	α_i (cm^{-1})	η_i (%)	$J_{th,\infty}$ (A/cm^2)
H	1.87	4.2	63	141
G	1.94	6.1	77	121
F	2.13	6.1	77	105
E	2.21	7.7	78	108
D	2.23	7.6	72	110
C	2.30	4.1	50	154
B	2.31	4.6	38	304
A	2.34	2.7	42	164

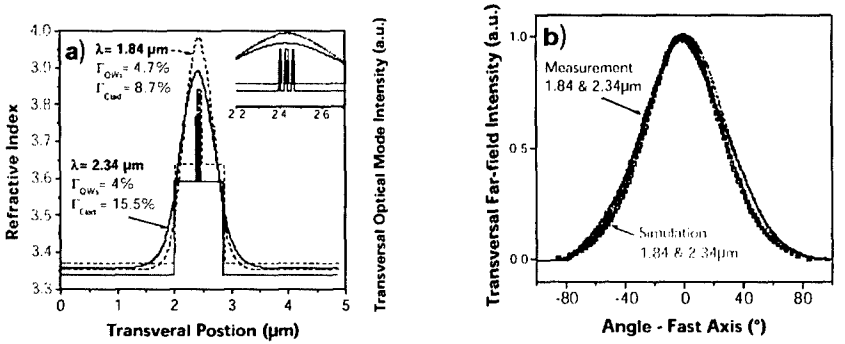

Figure 11. a) Calculated transversal optical mode intensity (right axis) and refractive index (left axis) vs transversal position, corresponding to the growth direction, for two different lasers emitting at 1.84 μm and 2.34 μm. The inset zooms in the QW active region; b) Calculated (symbols) and measured (line) transversal far-field angular distributions for two different lasers emitting at 1.84 μm and 2.34 μm.

The lateral optical field was calculated for a diode laser emitting at 1.94 μm with 16 μm wide ridge geometry. Figure 12 a) displays the calculated lateral optical mode profile (right axis) up to the 2nd order, together with the effective refractive index (left axis) reflecting the rectangular shape of the 16 μm ridge aperture. In contrast to the transversal pattern, however, the lateral FF shows a multi-mode behavior. Upon increasing the injection current, the profile shape changes, showing higher order side peaks, and the FWHM of the divergence angle increases somewhat from 4.8° ($2I_{th}$) to 5.6° ($4I_{th}$). Figure 12 b) illustrates the angular dispersion of the measured (upper) and simulated (lower) lateral

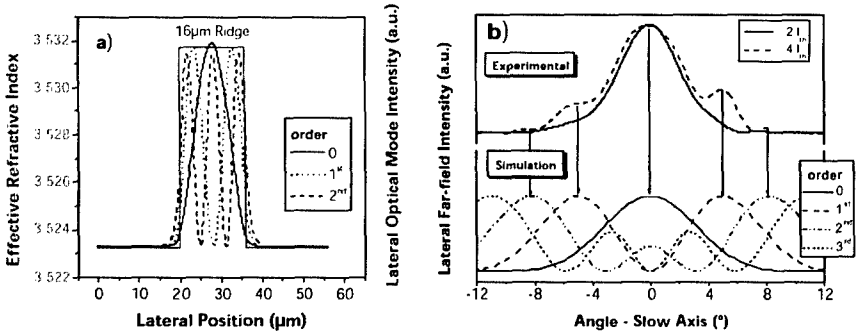

Figure 12. a) Calculated lateral optical mode spatial profiles up to the 2nd order for a 1.94 μm diode laser. The assumed etch depth is 1.9 μm and the ridge width is 16 μm; b) Experimental (upper) and calculated (lower) lateral far-field mode profiles of a 16 μm x 1000 μm diode laser with coated mirror facets emitting at 1.94 μm. The experimental data were recorded at room temperature for two different injection currents, $2I_{th}$ and $4I_{th}$, and the calculated angular distribution is up to the 3rd order.

FF intensities of the 1.94 μm diode laser with 16 μm ridge width and 1000 μm cavity length. The measurements have been performed again at $2I_{th}$ and $4I_{th}$. The angular dependence of the lateral FF was calculated up to the 3rd order mode. Regarding the measured profiles, at $2I_{th}$ only the zero order mode is visible in the experimental FF profile, whereas at $4I_{th}$ the first and second order modes are clearly resolved. The angular position of the measured side peaks originating from higher order modes is in excellent agreement with the calculations.

To fully exploit the superior material quality of the present (AlGaIn)(AsSb) diode lasers emitting around 2 μm, broad area lasers with single ended output have been processed, and mounted epi-side down for improved heat sinking. Resulting room-temperature cw optical output and total power efficiency versus injection current is depicted in Figure 13, for a 150 μm x 1000 μm broad area laser with emission wavelength of 1.98 μm at 300 K. A maximum cw output power exceeding 1.7 W at room temperature was achieved at a drive current of 6.8 A, corresponding to a voltage drop of 1.67 V. The maximum total power efficiency amounted to 27% and decreased to a value of 15% at the maximum power of 1.7 W.

CONCLUSIONS

GaInAsSb/AlGaAsSb type-I QW lasers spanning the spectral range from 1.74 to 2.34 μm have been realized and investigated. Laser structures with 3-QWs and SQW have been studied in detail. Excellent laser performances, which become evident from high characteristic temperatures T_O of 179 K, high internal quantum efficiency of 77%, and low internal losses of 6 cm^{-1}, have been achieved. Beside that, a comparison between the 3-QW and SQW laser structures showed that the threshold current density at infinite cavity and the transparency current density scale nicely with the number of QWs. A careful study has been conducted regarding the characteristic temperature of the threshold current with respect to the lasing wavelength in order to provide better understanding concerning the different loss mechanisms limiting the laser performances. An additional topic we have addressed was the investigation of the far field profiles related with these laser structures. Finally, 1.7 W cw optical output

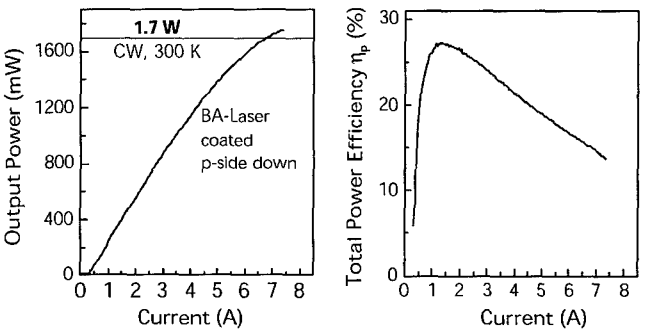

Figure 13. Room temperature cw output power vs current and total power efficiency vs current for 1.98 μm broad area diode lasers, coated and mounted epi-side down. Output powers exceeding 1.7 W cw have been achieved.

power at room temperature has been demonstrated using single ended broad area diode laser, a very promising result for high power applications of the 2 μm diode lasers.

ACKNOWLEDGMENTS

The authors would like to thank N. Herres and H. Güllich for HRXRD measurements, as well as M. Maier and T. Fuchs for SIMS analyses. Continuous support and encouragement by G. Weimann is gratefully acknowledged. This work was supported by the German Ministry for Education and Research (BMBF).

REFERENCES

1. G. W. Turner and H. K. Choi, in *Optoelectronic Properties of Semiconductors and Superlattices*, edited by M. O. Manasreh, (Gordon and Breach, Amsterdam, 1997), p. 369, and references therein.
2. D. Z. Garbuzov, R. U. Martinelli, H. Lee, P. K. York, R. J. Menna, J. C. Connolly, and S. Y. Narayan, Appl. Phys. Lett. **69**, 2006 (1996).
3. G. W. Turner, H. K. Choi, and M. J. Manfra, Appl. Phys. Lett. **72**, 876 (1998).
4. D. Z. Garbuzov, R. U. Martinelli, H. Lee, R. J. Menna, P. K. York, L. A. DiMarco, M. G. Harvey, R. J. Matarese, S. Y. Narayan, and J. C. Connolly, Appl. Phys. Lett. **70**, 2931 (1997).
5. T. Newell, X. Wu, A. L. Gray, S. Dorato, H. Lee, and L. F. Lester, IEEE Photon. Technol. Lett. **11**, 30 (1999).
6. D. A. Yarekha, G. Glastre, A. Perona, Y. Rouillard, F. Genty, E. M. Skouri, G. Boissier, P. Grech, A. Joullie, C. Alibert, and A. N. Baranov, Electron. Lett. **36**, 537 (2000).
7. D. Z. Garbuzov, H. Lee, V. Khalfin, R. Martinelli, J. C. Connolly, and G. L. Belenky, IEEE Photon. Technol. Lett. **11**, 794 (1999).
8. S. Simanowski, N. Herres, C. Mermelstein, R. Kiefer, J. Schmitz, M. Walther, J. Wagner, and G. Weimann, J. of Crystal Growth **209**, 15 (2000).
9. S. Simanowski, C. Mermelstein, M. Walther, N. Herres, R. Kiefer, M. Rattunde, J. Schmitz, J. Wagner, and G. Weimann, J. of Crystal Growth **227-228**, 595 (2001).
10. C. Mermelstein, S. Simanowski, M. Mayer, R. Kiefer, J. Schmitz, M. Walther, and J. Wagner, Appl. Phys. Lett. **77**, 1581 (2000).
11. M. Rattunde, C. Mermelstein, S. Simanowski, J. Schmitz, R. Kiefer, N. Herres, F. Fuchs, M. Walther, and J. Wagner, in *Proc. of the 27th Int. Symp. on Compound Semiconductors*, (Institute of Electrical and Electronics Engineers, Inc., USA, 2001) p. 437.
12. M. P. C. M. Krijn, Semicond. Sci. Technol. **6**, 27 (1991).
13. R. W. H. Engelmann, C-L. Shieh, and C. Shu, in *Quantum Well Lasers*, edited by P. S. Zory, Jr., (Academic Press, San Diego, CA, 1993), p. 170.
14. P. W. A. Mc Ilroy, A. Kurobe, and Y. Uematsu, IEEE J. Quantum Electron. **21**, 1958 (1985).
15. H. Schneider and K. v. Klitzing, Phys. Rev. B **38**, 6160 (1988).
16. D. Garbuzov, M. Maiorov, H. Lee, V. Khalfin, R. U. Martinelli, and J. Connolly, Appl. Phys. Lett. **74**, 2990 (1999).